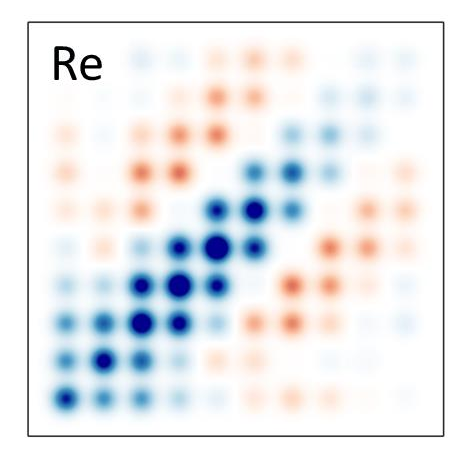
Time-Evolving Quantum Superpositions in Open Systems and the Rich Content of Coherence Maps

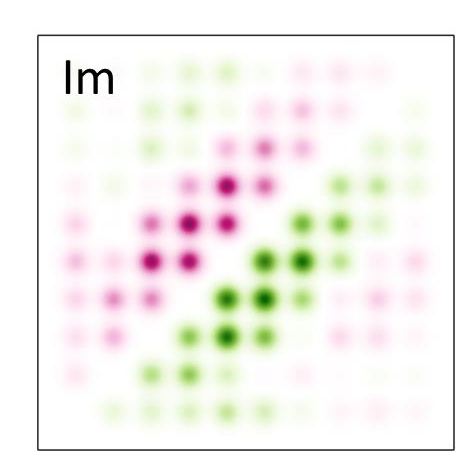
Reshmi Dani¹ and Nancy Makri^{*1,2,3}

¹Department of Chemistry, University of Illinois, Urbana, Illinois 61801

Abstract

We discuss general features of the time-evolving reduced density matrix (RDM) of multistate systems coupled to dissipative environments. We show that many important aspects of the dynamics are visualized effectively and transparently through coherence maps, i.e. snapshots of the real and imaginary components of the RDM on the square grid of system sites. In particular, the spread, signs, and shapes of the coherence maps collectively characterize the state of the system, the nature of the dynamics, as well as the equilibrium state. The topology of the system is readily reflected in its coherence map. Rows and columns show the composition of quantum superpositions and their filling indicates the extent of surviving coherence. Linear combinations of imaginary RDM elements specify instantaneous population derivatives. The main diagonal comprises the incoherent component of the dynamics, while the upper/lower triangular areas give rise to coherent contributions that increase the purity of the RDM. In open systems the coherence map evolves to a band surrounding the principal diagonal whose width decreases with increasing temperature and dissipation strength. We illustrate these behaviors with examples of 10-site model molecular aggregates with Frenkel exciton couplings, where the electronic states of each monomer are coupled to harmonic vibrational baths.





²Department of Physics, University of Illinois, Urbana, Illinois 61801

³Illinois Quantum Information Science and Technology Center, University of Illinois, Urbana, Illinois 61801

^{*}Corresponding author. Email: nmakri@illinois.edu

1. Introduction

A number of major advances in experimental tools over the last two decades, in particular nonlinear (two-dimensional electronic¹⁻⁴ and two-dimensional electronic-vibrational⁵) spectroscopy,⁶⁻⁷ have led to a wealth of information on the quantum dynamics of many processes, such as charge and energy transfer, in condensed phase and biological environments. On the theoretical side, several developments in methodology have enabled accurate simulation of time-dependent properties in a variety of quantum mechanical systems.

The complex behaviors of time-evolving quantum mechanical systems interacting with condensed phase environments is encoded in the reduced density matrix⁸⁻⁹ (RDM) and in time correlation functions.¹⁰ The latter are usually evaluated with respect to the equilibrium density matrix and often can infer nonequilibrium behaviors under certain assumptions such as the regression hypothesis of linear response.¹¹⁻¹³ For example, flux correlation functions yield reaction rates,¹⁴ velocity correlation functions are related to diffusion constants,¹³ and dipole moment correlation functions are used to calculate spectra.⁶⁻⁷ The RDM is useful for directly simulating processes far from equilibrium. Typically, simulations report various state populations which characterize the transformation of a system from a particular initial preparation to the final product. With the exception of spin dynamics^{8,15} and the magnetic resonance literature, off-diagonal elements of the RDM have not received as much attention in chemical dynamics simulation, although it is known that they carry important information related to coherence properties and nonlinear spectra; for this reason, the off-diagonal elements of the RDM are often referred to as "coherences".

Quantum coherence has been the focus of intense investigations, motivated in part by the quest for directing processes to desired products inaccessible to classical pathways. Depending on the context and the chosen basis, quantum coherence manifests itself in many different ways. For example, quantum coherence is intimately tied to superpositions, which characterize not only evolving quantum systems but also eigenstates of the Hamiltonian in a local basis. These different situations have distinct manifestations, and their characteristics are important for elucidating complex dynamical processes.

In this paper we discuss and illustrate the rich information encoded in coherences. First, using simple quantum mechanics, we describe the relationships between coherences and various properties of interest. Systems comprising multiple states have many off-diagonal RDM elements. We show that snapshots of the *coherence map* (a contour plot of all real and imaginary components of the RDM on the square grid of system states) convey a wealth of information and many physical insights. The spread, signs, and shapes of the coherence maps *collectively* characterize the state of the system, the nature of the dynamics, as well as the equilibrium state.

We begin by describing some general characteristics of the RDM of a time-evolving quantum superposition and discuss how instantaneous rates are related to coherences and the nature of equilibrium distribution obtained in the long-time limit. Next, we present the time evolution of coherence maps for several systems comprising 10 states, in linear and ring arrangements, with local and next-nearest-neighbor couplings, isolated and coupled to harmonic baths with weak or moderate strength at two temperatures, and with site-localized or eigenstate initial conditions. We analyze the features of these maps, highlight their differences, and discuss the physical insights that can be derived from these images. The chosen models and range of parameters are representative of excitation energy transfer in natural and artificial molecular aggregates, and the obtained results allow us to highlight common and contrasting patterns. These

illustrations help establish useful benchmarks for understanding the time evolution of complex systems and to correlate the features of coherence maps to important topological, structural and electronic/vibrational characteristics.

In section II we describe the features the RDM and their signatures in the coherence map. In section III we show snapshots of coherence maps for a variety of 10-state systems coupled to model vibrational baths. These results are obtained through a numerically exact implementation of the path integral formulation of quantum dynamics¹⁶⁻¹⁷ and are free of dynamical approximations or assumptions. We summarize in section IV with some concluding remarks.

2. General features of coherence maps

We consider a discrete system with n sites $|\varphi_i\rangle$, which is described by the Hamiltonian

$$\hat{H}_0 = \sum_{i=1}^n \sum_{j=1}^n H_{ij} \left| \varphi_i \right\rangle \left\langle \varphi_j \right|. \tag{2.1}$$

This form is the most general tight binding Hamiltonian. In many physical situations the sites correspond to donor/bridge/acceptor electronic states of charge transfer systems or monomer excited states in molecular aggregates. The n eigenstates of the system are obtained from the eigenvalue equation

$$\hat{H}_0 | \Phi_k \rangle = E_k | \Phi_k \rangle, \quad k = 0, 1, \dots, n-1.$$

$$(2.2)$$

In general, the system interacts with a large environment of vibrational, phonon, solvent, or biomolecular medium degrees of freedom (the "bath") at a given temperature. The RDM of the system (in the site representation) is given by

$$\tilde{\rho}_{km}(t) = \operatorname{Tr}_{b} \langle \varphi_{k} | e^{-i\hat{H}t/\hbar} \hat{\rho}(0) e^{i\hat{H}t/\hbar} | \varphi_{m} \rangle$$
(2.3)

where $\hat{\rho}(0)$ is the initial density operator and the trace is with respect to the bath. In this section we do not impose any restrictions on the form of the bath Hamiltonian or the initial density matrix.

We define the coherence map as the complex-valued surface of RDM values on the square $n \times n$ grid of system sites at a particular time. In this section we discuss various universal properties of coherence maps. In the next section we show the real and imaginary components side-by-side.

(i) Pure states

Often the system is initially uncorrelated from the bath (i.e. the full density matrix is a product of system and bath components), and the system is in a pure state, i.e.

$$\tilde{\rho}(0) = |\Psi(0)\rangle\langle\Psi(0)| \tag{2.4}$$

In the absence of coupling to a bath, the evolution is unitary and thus the system remains indefinitely in a pure state, i.e.

$$\tilde{\rho}(t) = |\Psi(t)\rangle\langle\Psi(t)| \tag{2.5}$$

where $|\Psi(t)\rangle$ satisfies the time-dependent Schrödinger equation. Expressing the time-evolving state in the site basis,

$$|\Psi(t)\rangle = \sum_{i=1}^{n} c_i(t) |\varphi_i\rangle$$
 (2.6)

the RDM becomes

$$\tilde{\rho}_{km}(t) = c_k(t)c_m^*(t) \tag{2.7}$$

In this case the RDM describes a time-evolving superposition state and, in general, many (or all) of the coefficients have nonzero values at any time. Because the RDM of a pure state factorizes, its rows (and columns) are proportional to one another, i.e.

$$\frac{\tilde{\rho}_{k'm}(t)}{\tilde{\rho}_{k''m}(t)} = \frac{c_{k'}(t)}{c_{k''}(t)}, \quad m = 1, \dots, n.$$
(2.8)

Figure 1 illustrates this relation for a 10-site system (with the parameters of Figure 3 a,b shown in the next section) and its breakdown in the case where the system is coupled to a bath.

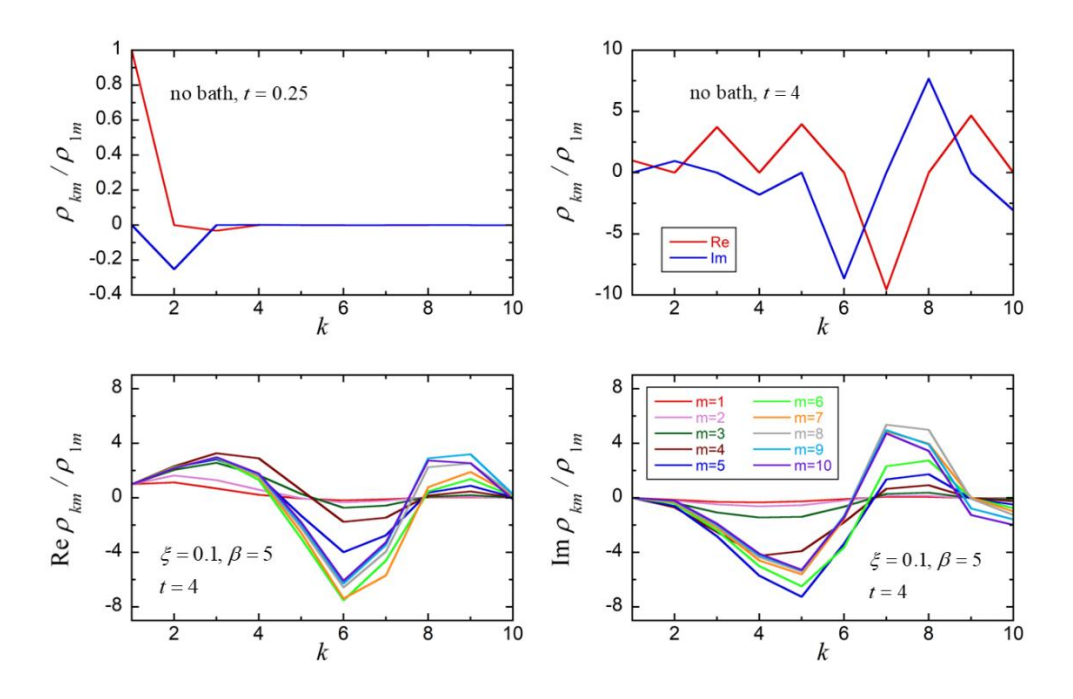


Fig. 1. Composition of quantum superpositions. The ratio $\tilde{\rho}_{km}$ / $\tilde{\rho}_{lm}$ is shown for all values of k for a 10-site chain. Top: isolated system. The lines show real and imaginary components of the ratio at two times. The ratios for all k values are indistinguishable. Bottom: system with sites coupled to harmonic baths with $\xi = 0.1$, $\beta = 5$. The left panel shows the real part while the right shows the imaginary part of the ratio at t = 4.

Thus, all rows (or columns) encode the same information in this case, and the RDM has rank equal to unity. Each column of such a RDM contains (apart from a multiplicative constant) the coefficients that describe the instantaneous quantum superposition state that has evolved from the chosen initial condition. If a single site is occupied initially, unitary evolution will rapidly create superpositions that span multiple sites and the RDM will spread.

(ii) Dissipative evolution

When the system is coupled to a large environment, the evolution of the RDM is no longer unitary. As a result, an initially pure state evolves into a mixture. In this case each row (or column) of the RDM is a weighted sum of multiple quantum superpositions. For example, when equilibrium is reached at a finite temperature, the RDM is an incoherent sum of Boltzmann-weighted eigenstates. The effect is different in each row, removing the linear dependence observed for pure states and increasing the rank of the RDM. The destructive interference that occurs destroys (to some extent or entirely) the quantum superposition and leads to the partial or complete localization of the RDM.

We note that the localization need not develop monotonically with time, i.e. the RDM may initially localize considerably and later spread out again. Further, while dissipation destroys early-time superpositions, entirely new superpositions may form as time progresses. These intriguing behaviors are visually conveyed in a clear and insightful way in the coherence maps.

(iii) Long-time properties

When the system is coupled to a dissipative bath, the RDM elements eventually settle to their equilibrium values, which are given by the Boltzmann matrix (traced with respect to the bath):

$$\lim_{t \to \infty} \tilde{\rho}_{km}(t) = Z^{-1} \operatorname{Tr}_{b} \langle \varphi_{k} | e^{-\beta \hat{H}} | \varphi_{m} \rangle$$
(2.9)

where $\beta = 1/k_BT$ and Z is the partition function. The Boltzmann matrix is purely real-valued, thus the imaginary parts of $\tilde{\rho}_{km}(t)$ always vanish at long times. In the absence of a bath, the RDM elements oscillate indefinitely and a long-time limit does not exist.

Under very weak system-bath coupling, the projections of the system-bath eigenstates on the subspace of the system closely resemble the eigenstates of the bare system. In this case the RDM equilibrates to values given (to a very good approximation) by the Boltzmann matrix of the bare system, i.e.,

$$\lim_{\substack{t \to \infty \text{weak coupling} \\ \text{to be the probable}}} \tilde{\rho}_{km}(t) = Z_0^{-1} \langle \varphi_k | e^{-\beta \hat{H}_0} | \varphi_m \rangle. \tag{2.10}$$

In the limit of zero temperature ($\beta \to \infty$) only the ground state of the system is populated, thus

$$\lim_{\substack{t \to \infty, \ \beta \to \infty \text{ weak coupling} \\ \text{to bath}}} \tilde{\rho}_{km}(t) = \langle \varphi_k | \Phi_0 \rangle \langle \Phi_0 | \varphi_m \rangle \tag{2.11}$$

In this case, the RDM spreads over the entire set of sites spanned by the system ground state. While populations are always positive, the signs of the coherences depend on the character of the ground state. In most common situations the ground state wavefunction is nodeless, but eigenvector signs can be reversed by changing the signs of Hamiltonian elements. Thus, coherences may retain alternating signs in the long time limit at low-temperatures.

As the temperature is increased, multiple eigenstates begin to contribute to the RDM, thus

$$\lim_{\substack{t \to \infty \text{ weak coupling}}} \tilde{\rho}_{km}(t) = Z_0^{-1} \sum_{j=0}^{n-1} e^{-\beta E_j} \left\langle \varphi_k \left| \Phi_j \right\rangle \left\langle \Phi_j \left| \varphi_m \right\rangle \right.$$
 (2.12)

The destructive interference leads to decreased values of off-diagonal elements, erasing signs and effectively decreasing the spread of the coherence map. If only nearby sites are coupled in the Hamiltonian, the coherence map is dominated by a band centered about the main diagonal. In the infinite temperature limit only the main diagonal of the RDM is populated.

As the system-bath coupling is increased, the multidimensional eigenstates become strongly non-factorizable and thus their projections on the subspace of the system no longer resemble the eigenstates of the bare system. This leads to significant deviations from the patterns discussed above. With moderate-to-strong system-bath coupling, the effects of the bath are similar to those of temperature. Thus, the RDM tends to be localized on a band surrounding the main diagonal of the coherence map. The width of this band is associated with the quantum dispersion of the system at the given temperature.

(iv) Imaginary components of coherences

In recent work¹⁸ we showed that the rate of population change is related to the imaginary parts of the coherences through the expression

$$\frac{d}{dt}\tilde{\rho}_{kk}(t) = \frac{2}{\hbar} \sum_{i=1}^{n} H_{jk} \operatorname{Im} \tilde{\rho}_{jk}(t), \qquad (2.13)$$

where H_{jk} are the matrix elements of the bare system Hamiltonian, Eq. (2.1). Eq. (2.13) is exact, regardless of the form of the bath Hamiltonian, as long as the system-bath coupling is diagonal in the system basis. This relation shows that a site population can have a nonzero derivative, i.e. can be growing or decreasing, only if there exist at the given instant quantum superpositions between this site and other sites to which it couples through the system Hamiltonian. Further, superpositions must have imaginary components in order to drive population changes. In the absence of imaginary components in the coherences, site populations

remain stationary. Even in high-temperature, strong-dissipation regimes of "incoherent" population dynamics, time evolution is still governed by quantum superpositions. As the system dynamics approaches equilibrium, the imaginary terms gradually die out and population evolution ceases. Although strong quantum superpositions often survive even at equilibrium, they are purely real-valued.

Oscillatory population dynamics implies rapidly changing populations of two or more sites. Large time derivatives, of magnitude comparable to those during the initial part of the evolution, are sustained over long times. This requires the existence of persisting, intense imaginary components in the RDM at least on the locations of nonzero coupling elements.

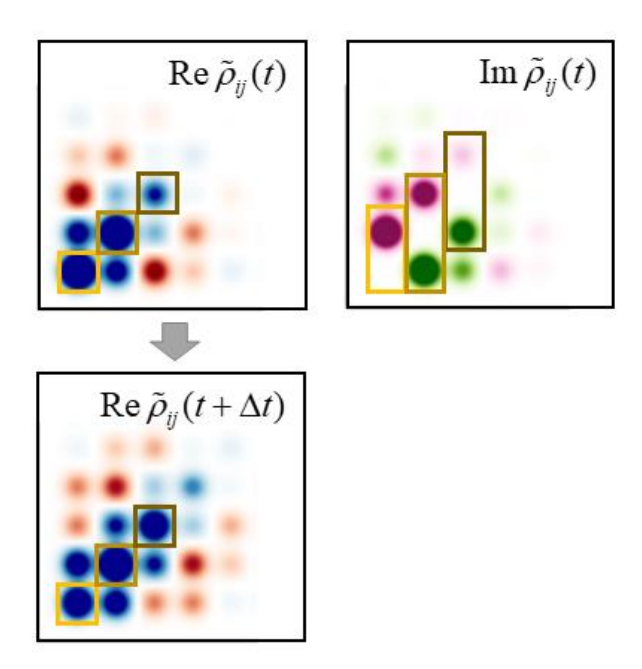


Fig. 2. Illustration of the relation between population derivatives and imaginary components of coherences. The top panel shows the real (left) and imaginary (right) parts of the RDM for a multisite tight binding system with negative nearest-neighbor couplings, weakly coupled to a low-temperature bath at an early time. Blue/red and magenta/green indicate positive and negative regions, respectively. The time derivative of $\tilde{\rho}_{11}$ (yellow square) is determined by the coherence in the yellow rectangle, which upon multiplication with the negative coupling gives a negative value. The time derivatives of $\tilde{\rho}_{22}$ and $\tilde{\rho}_{33}$ (gold and brown squares) are determined by the coherences in the gold and brown rectangles. It is seen that the time derivative of $\tilde{\rho}_{22}$ is close to zero, while that of $\tilde{\rho}_{33}$ is positive. This implies that $\tilde{\rho}_{11}$ is decreasing, while $\tilde{\rho}_{22}$ is close to an extremum and $\tilde{\rho}_{33}$ is growing. The lower panel shows the real part of the RDM a short time later, confirming that $\tilde{\rho}_{11}$ has decreased, $\tilde{\rho}_{22}$ has not changed much and $\tilde{\rho}_{33}$ has increased.

(v) Purity and entropy

The purity of the RDM,

$$Q(t) = \text{Tr} \left[\tilde{\rho}(t)^2 \right], \tag{2.14}$$

contains useful information which is similar to that conveyed by of von Neumann entropy¹⁹ but has a simpler algebraic form. Eq. (2.14) becomes

$$Q(t) = \sum_{i=1}^{n} \sum_{j=1}^{n} \tilde{\rho}_{ij}(t) \tilde{\rho}_{ji}(t) = \sum_{i=1}^{n} \sum_{j=1}^{n} \left| \tilde{\rho}_{ij}(t) \right|^{2} = \sum_{i=1}^{n} \tilde{\rho}_{ii}(t)^{2} + 2 \sum_{i=1}^{n} \sum_{j>i}^{n} \left| \tilde{\rho}_{ij}(t) \right|^{2} = Q_{\text{incoh}}(t) + Q_{\text{coh}}(t)$$
(2.15)

where

$$Q_{\text{incoh}}(t) = \sum_{i=1}^{n} \tilde{\rho}_{ii}(t)^{2},$$

$$Q_{\text{coh}}(t) = 2\sum_{i=1}^{n} \sum_{j>i}^{n} |\tilde{\rho}_{ij}(t)|^{2} = 2\sum_{i=1}^{n} \sum_{j>i}^{n} (\operatorname{Re} \tilde{\rho}_{ij}(t))^{2} + 2\sum_{i=1}^{n} \sum_{j>i}^{n} (\operatorname{Im} \tilde{\rho}_{ij}(t))^{2}$$
(2.16)

The incoherent component is the sum of the squared populations. If many sites are significantly populated, norm conservation implies that this term is small. For example, if all n sites of the system are equally populated, the incoherent component of purity is 1/n.

The spreading of populations on all sites does not necessarily imply a strongly mixed state, because the coherent term may increase the purity to unity. The coherent contribution is the sum of squared real and imaginary components of the coherences, i.e. (twice the) sum of squared elements in the lower triangles of the real and imaginary coherence maps. At equilibrium the imaginary components vanish, thus the purity of the RDM depends on the real-valued coherences. As the temperature and/or damping through the bath is increased, the spread of the RDM evolves into a band surrounding the main diagonal while the other corners of the coherence map have very low values. This situation corresponds to a highly mixed RDM. At equilibrium and under strongly incoherent conditions (high temperature, strong system-bath coupling) the RDM becomes diagonal with all site populations equal to 1/n, thus only the incoherent term contributes and the purity takes its minimum value of 1/n. In the case of a two-level system (TLS, n = 2), the real part of the RDM element is related to the difference of eigenstate populations, while the imaginary part is proportional to the instantaneous transfer rate.

3. Coherence maps for Frenkel exciton molecular aggregate models coupled to harmonic baths

In this section we illustrate the relations and features described in section II on representative Frenkel exciton systems, $^{23-24}$ where the Hamiltonian has a tight-binding form comprising the single excitation manifold of molecular aggregates and each site is coupled to a model harmonic bath that provides dissipative effects typical of exciton-vibration interactions. The model systems involve linear and circular aggregates of n = 10 degenerate sites, coupled via nearest-neighbor (nnn) or nearest-plus next-nearest-neighbor (nnn) terms according to the Hamiltonians

$$\hat{H}_{0}^{\text{chain}} = \sum_{i=1}^{n-1} J_{\text{nn}} \left(\left| \varphi_{i} \right\rangle \left\langle \varphi_{i+1} \right| + \left| \varphi_{i+1} \right\rangle \left\langle \varphi_{i} \right| \right) + \sum_{i=1}^{n-2} J_{\text{nnn}} \left(\left| \varphi_{i} \right\rangle \left\langle \varphi_{i+2} \right| + \left| \varphi_{i+2} \right\rangle \left\langle \varphi_{i} \right| \right)$$

$$\hat{H}_{0}^{\text{ring}} = \hat{H}_{0}^{\text{chain}} + J_{\text{nn}} \left(\left| \varphi_{N} \right\rangle \left\langle \varphi_{1} \right| + \left| \varphi_{1} \right\rangle \left\langle \varphi_{N} \right| \right)$$

$$+ J_{\text{nnn}} \left(\left| \varphi_{N} \right\rangle \left\langle \varphi_{2} \right| + \left| \varphi_{2} \right\rangle \left\langle \varphi_{N} \right| \right) + J_{\text{nnn}} \left(\left| \varphi_{N-1} \right\rangle \left\langle \varphi_{1} \right| + \left| \varphi_{1} \right\rangle \left\langle \varphi_{N-1} \right| \right)$$

$$(3.1)$$

where $J_{\rm nn}$ and $J_{\rm nnn}$ are the nearest- and next-nearest-neighbor coupling parameters with $J_{\rm nnn}=0$ or $J_{\rm nnn}=\frac{1}{2}J_{\rm nn}$. The magnitude of $J_{\rm nn}$ sets the main time scale of the system dynamics. We set $|J_{\rm nn}|=1$, such

that the time label in the figures is in units of $\hbar/|J_{\rm nn}|$ and the inverse temperature is in units of $J_{\rm nn}^{-1}$. The sign of the coupling term is governed by the stacking of the molecular units, and we consider both signs of nearest-neighbor coupling. With $J_{\rm nn}<0$, the ground state of the system Hamiltonian is nodeless. This is the most common situation, encountered in the exciton coupling of J aggregates (and also in the *p*-orbital interactions of aromatic compounds). In contrast, the tight-binding Hamiltonian with $J_{\rm nn}>0$ has a ground state with alternating signs and is characteristic of H aggregates.²⁵

To mimic the singly excited subspace of a J or H aggregate,²⁵ each site of the system is coupled to its own harmonic bath.²⁶⁻²⁷ The system-bath coupling term is

$$\hat{H}_{sb} = \left(\hat{h}_i^1 + \sum_{j \neq i} \hat{h}_i^0 \right) |\varphi_i\rangle \langle \varphi_i|, \qquad (3.2)$$

where

$$\hat{h}_{i}^{0} = \sum_{k} \left(\frac{\hat{p}_{ik}^{2}}{2m} + \frac{1}{2} m \omega_{k}^{2} \hat{q}_{ik}^{2} \right), \quad \hat{h}_{i}^{1} = \sum_{k} \left(\frac{\hat{p}_{ik}^{2}}{2m} + \frac{1}{2} m \omega_{k}^{2} \left(\hat{q}_{ik} - \frac{2c_{k}}{m \omega_{k}^{2}} \right)^{2} \right)$$
(3.3)

Here \hat{q}_{ik} , \hat{p}_{ik} are the coordinate and momentum of bath mode k associated with site i. All sites are coupled to identical baths with frequencies ω_k and coupling constants c_k , which are collectively characterized by the spectral density function²⁸⁻²⁹

$$J(\omega) = \frac{1}{2} \pi \xi \omega e^{-\omega/\omega_{c}} \tag{3.4}$$

This function peaks at the frequency ω_c , where ξ is the dimensionless Kondo parameter that quantifies the system-bath coupling strength. The reorganization energy of each monomer is given by $\lambda = 2\xi\hbar\omega_c$.

We choose bath parameters that are representative of natural and synthetic molecular aggregates. However, we emphasize that real molecular systems have vibrational modes with frequencies and Huang-Rhys factors that are unevenly distributed, and their precise forms can give rise to distinct behaviors. In the present work we choose $\omega_{\rm c}=5$ (in units of $|J_{\rm nn}|$) and two site-bath coupling values, $\xi=0.1$ and 0.3, which give rise to vibrational reorganization energies equal to 1 and 3, respectively (again, in units of $|J_{\rm nn}|$). For reference, electronic structure calculations have found the nearest-neighbor electronic couplings $J_{\rm nn}$ in the B850 ring of the bacterial LH2 complex to be 363 cm⁻¹, ³⁰ while the value -514 cm⁻¹ has been obtained³¹ for J aggregates of a perylene bisimide (PBI), ³² a promising molecule for solar energy harvest. The relevant intramolecular vibrational reorganization energies are 217 cm⁻¹ for the bacteriochlorophyll molecule and 879 cm⁻¹ for PBI. Thus, the model parameter we choose are in the relevant range, with $\xi=0.3$ being slightly large when judged on the basis of these two molecular systems.

In all cases the bath is initially equilibrated with respect to a common ground state $\sum_i \hat{h}_i^0$, as in the case of energy transfer following a Franck-Condon initial excitation.²⁷ We show results for an initial density localized on the first site (the edge of the chain), $\tilde{\rho}(0) = |\phi_1\rangle\langle\phi_1|$, and also for an eigenstate initial condition, $\tilde{\rho}(0) = |\Phi_m\rangle\langle\Phi_m|$. These results are representative of a variety of experimental situations and the results provide useful insights for the dynamics of energy transfer in molecular aggregates.

The calculations were performed using the small matrix path integral³³⁻³⁵ (SMatPI) methodology, an exact, analytically derived decomposition of the quasi-adiabatic propagator path integral³⁶⁻³⁹ (QuAPI). Both algorithms use the Feynman-Vernon influence functional⁴⁰ to integrate out the harmonic bath analytically at any temperature. These real-time path integral methods converge to numerically exact, fully quantum mechanical results and have been employed in many investigations of open quantum systems. In particular, the SMatPI decomposition circumvents the use of QuAPI tensors, storing only a few $n^2 \times n^2$ matrices. The low storage requirements of SMatPI make it ideal for application to multistate systems.

(i) Linear J aggregates with nearest-neighbor couplings, site-localized initial density

We begin with a linear chain of N=10 sites coupled by nearest-neighbor couplings $J_{\rm nn}=-1$, which describe J aggregates, and assume the initial density is localized on the first site, $\tilde{\rho}(0)=\left|\phi_1\right>\left<\phi_1\right|$. Figure 3 shows the populations of all sites as a function of time in the absence of coupling to a bath, for a weakly coupled bath at a low temperature ($\xi=0.1$, $\beta=5$), and for moderate system-bath coupling at an intermediate temperature ($\xi=0.3$, $\beta=1$). We note that even a weakly dissipative, low-temperature environment leads to drastic changes in the population dynamics, damping the oscillatory patterns characteristic of the isolated system.

Figures 4-6 show the coherence maps, i.e. the real and imaginary parts of the RDM, at select times for these parameters. In the absence of dissipative interactions (Fig. 4), the RDM for the nearest-neighbor tight binding system has real and imaginary parts that alternate along the chain, i.e. $\tilde{\rho}_{km}(t)$ is purely real-valued if k+m is an even number and purely imaginary if k+m is odd. The RDM spreads in a square pattern that forms 45° angles with the main axes, as density spreads to nearby sites, while coherences between sites of growing distance are formed. These coherences reflect the creation of quantum superpositions on multiple sites. As discussed in section II, all rows and columns of the coherence map at a given time correspond to the same superposition state, scaled by different multiplicative factors. This was most clearly seen in Figure 1, which shows the ratio $\tilde{\rho}_{km} / \tilde{\rho}_{lm}$ for all values of the site index k at a particular time in the absence of system-bath coupling. The population spreads over most sites very rapidly and, as the opposite end of the chain is reached, it accumulates there. Following reflection, the RDM fills the entire grid. Such spreading is one of the signatures of anharmonic systems characterized by multiple time scales. In this case of unitary evolution both real and imaginary parts of the RDM continue to evolve indefinitely, as the system cannot equilibrate. Overall, the magnitude of imaginary components does not decrease with time, as populations oscillate according to phases governed by the system eigenvalues.

Different patterns are observed when the sites are coupled to dissipative baths (Figures 5 and 6). The mixing of superposition states produced by the bath destroys the alternating real/imaginary structure of the RDM, and coherences are now complex-valued on all sites. The square-shaped evolution pattern observed in the case of the bare system is replaced by skewed shapes, which are elongated along the principal diagonal line of site populations. The spread of quantum superpositions, estimated from the length of visible coherence density in a particular row, varies considerably across different rows of the RDM. This is a consequence of the row-specific cancellation (and resulting superposition length) brought about by the incoherent summation of coherences induced by the bath. Further, the system eventually reaches equilibrium, thus (in contrast to the evolution of the bare system RDM shown in Fig. 4) the real parts of all RDM elements stabilize and the imaginary parts approach zero at long times. Imaginary components are seen to gradually decrease in magnitude, as system populations enter the interval of slow decay on their

approach to equilibrium values. In this pre-equilibrium phase the RDM elements are positive throughout the coherence map and concentrated within a band surrounding the principal diagonal, whose width changes over time. Specifically, the row width oscillates mildly as population maxima evolve, until these oscillations die out when the Boltzmann distribution is reached.

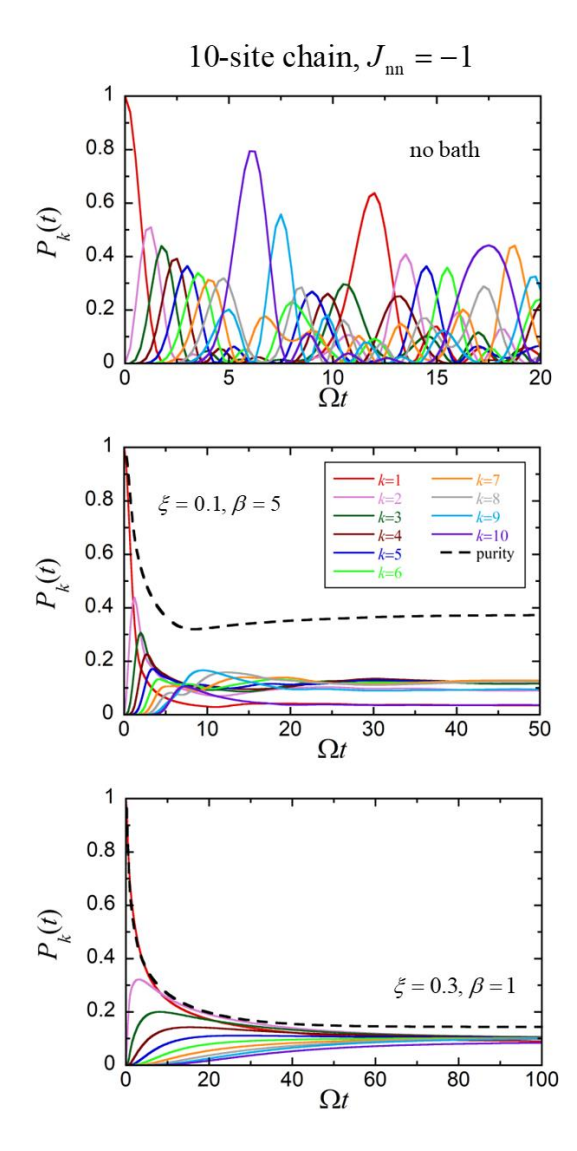


Fig. 3. Site populations and purity as a function of time in linear 10-site chains with nearest-neighbor couplings of strength $J_{nn}=-1$, where the sites are coupled to harmonic dissipative baths described in section III. The first site is initially populated. (a) Bare system dynamics ($\xi=0$). (b) Weak system-bath coupling at a low temperature ($\xi=0.1$, $\beta=5$). (c) Moderate system-bath coupling at an intermediate temperature ($\xi=0.3$, $\beta=1$).

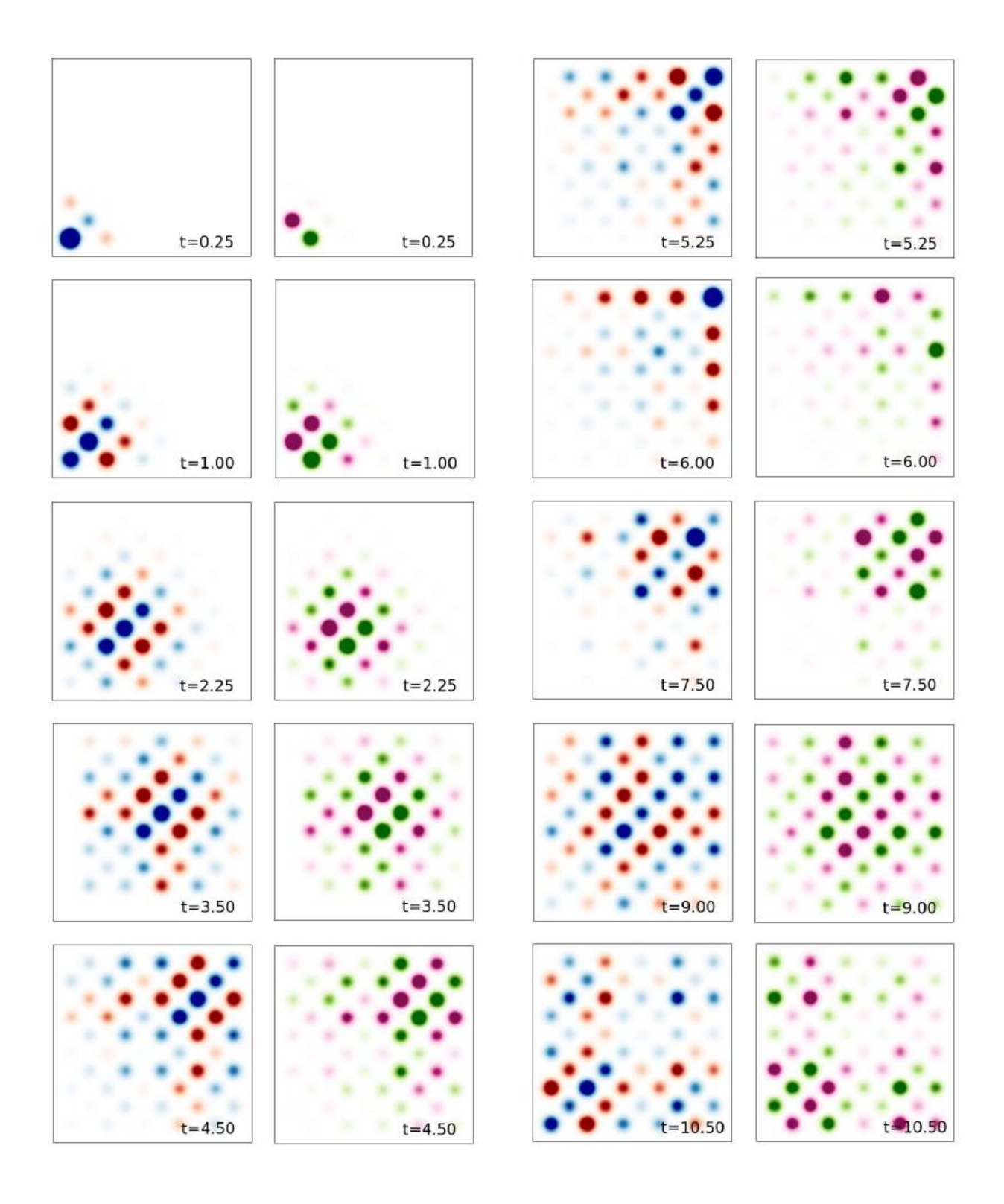


Fig. 4. Coherence maps for a 10-site chain described by Eq. (3.1) with $J_{\rm nn}=-1$ at various instants. The first site is initially populated. Blue and red colors correspond to positive and negative areas of the real part of the RDM, while magenta and green correspond to positive and negative areas of the imaginary part of the RDM.

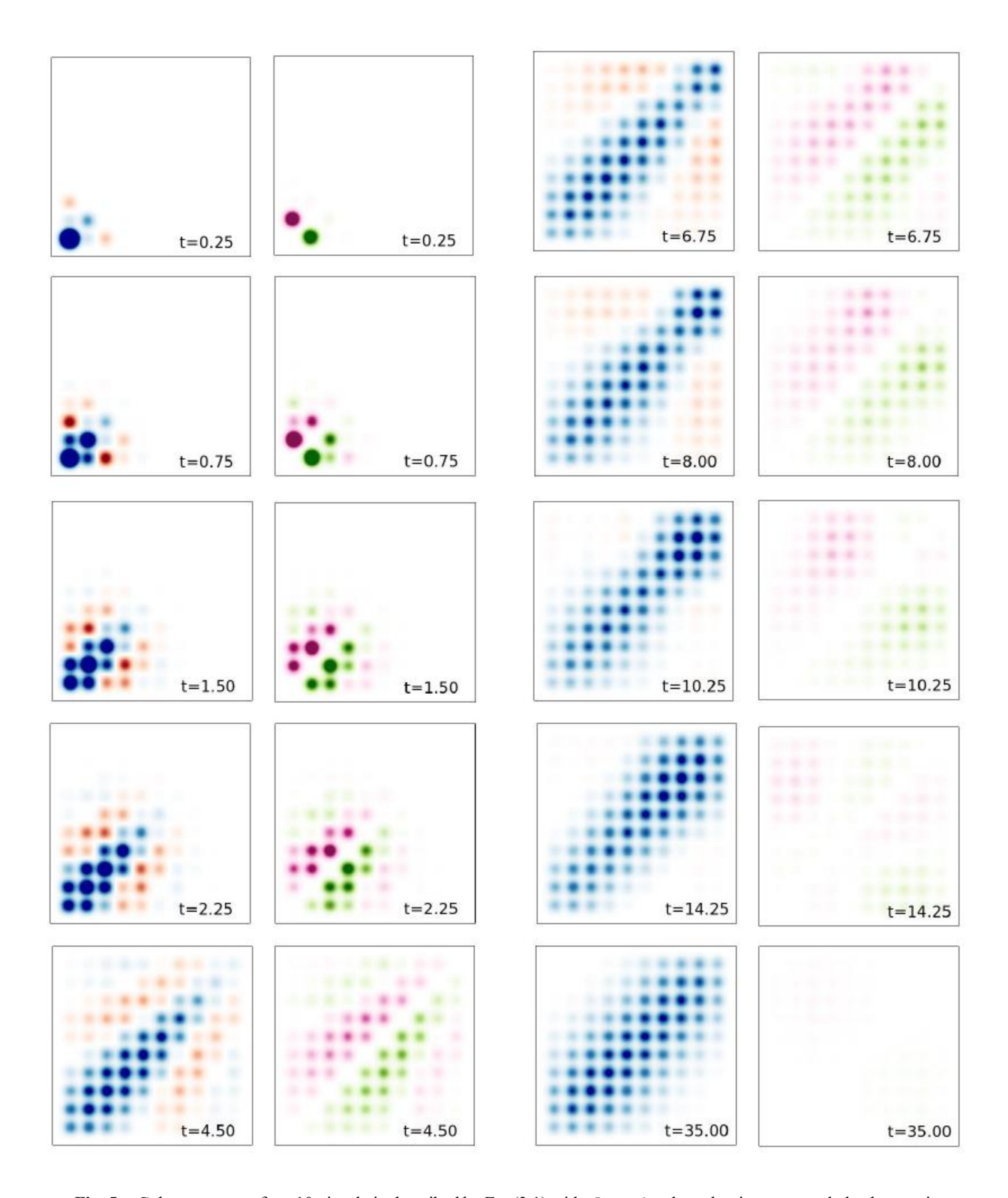


Fig. 5. Coherence maps for a 10-site chain described by Eq. (3.1) with $J_{\scriptscriptstyle \rm mn}=-1$, where the sites are coupled to harmonic bath with $\xi=0.1$ at an inverse temperature $\beta=5$, at various instants. The first site is initially populated. Blue and red colors correspond to positive and negative areas of the real part of the RDM, while magenta and green correspond to positive and negative areas of the imaginary part of the RDM.

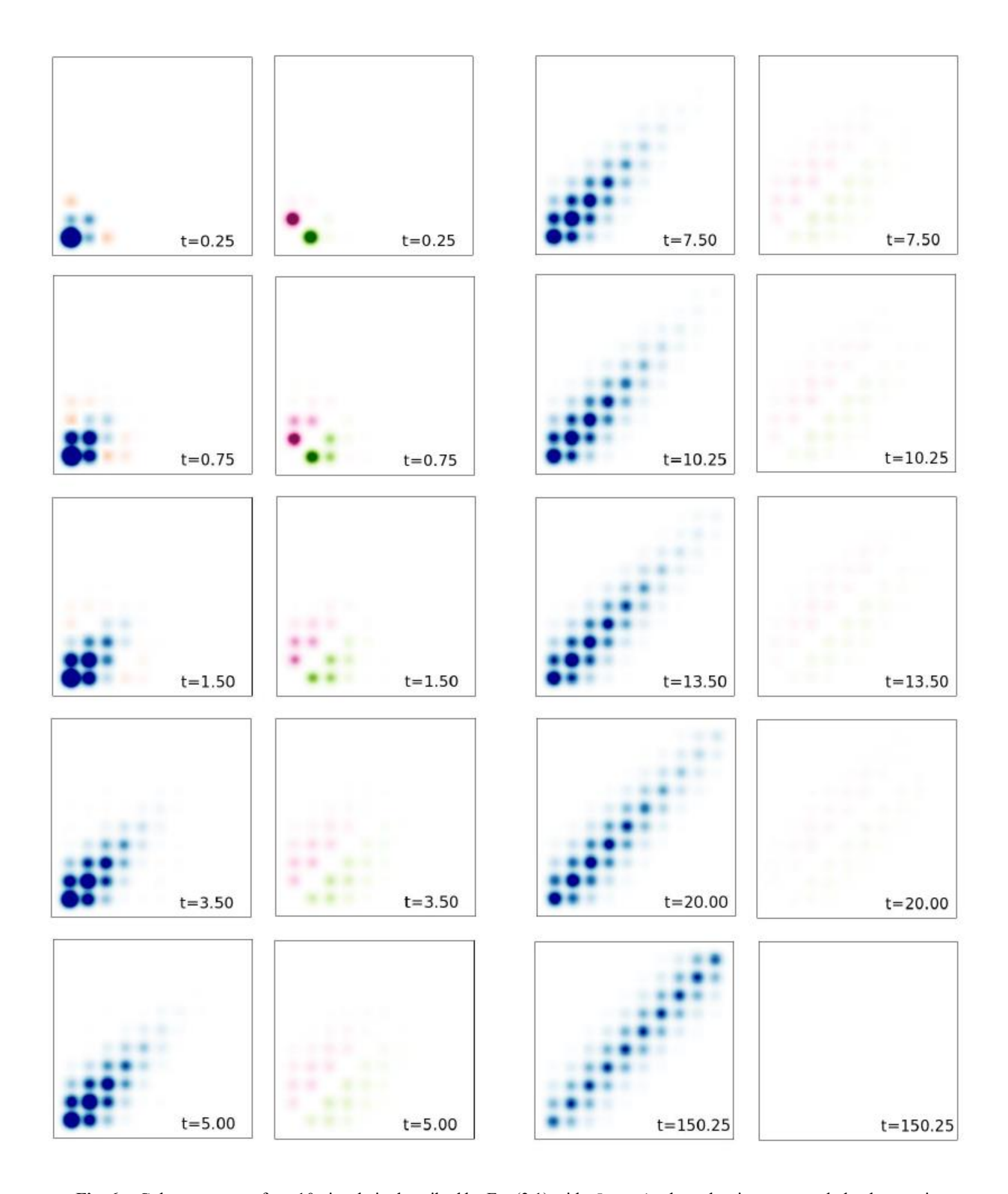


Fig. 6. Coherence maps for a 10-site chain described by Eq. (3.1) with $J_{\rm nn}=-1$ where the sites are coupled to harmonic baths with $\xi=0.3$ at an inverse temperature $\beta=1$, at various instants. The first site is initially populated. Blue and red colors correspond to positive and negative areas of the real part of the RDM, while magenta and green correspond to positive and negative areas of the imaginary part of the RDM.

Also shown in Fig. 3 is the purity of the RDM for the three parameter sets. In the absence of dissipative interactions, the evolution is unitary and the purity is preserved. In contrast, weak site-bath coupling is seen to significantly affect the purity, even at a low temperature, which decreases rapidly as neighboring sites are populated. This rapid mixing reflects primarily the incoherent contribution, which is associated with population spreading, and is countered by the spreading of the RDM in the direction perpendicular to the main diagonal, i.e. the creation of coherences. In the case of a weakly dissipative environment, the competition between incoherent and coherent contributions results in a shallow minimum of the purity curve at an intermediate time. As evolution continues, the coherent contribution from the growing coherences leads to a small increase of purity. Eventually only the imaginary components vanish and the only coherent contribution is the real-valued band. These behaviors have been observed and analyzed in the case of a two-level system (TLS), 20-22 where the rebound of the purity was seen to be very significant under low-temperature, weakly dissipative conditions. The multitude of time scales in the present 10-state system allow the coherence-quenching effects of the bath to be more prominent. In addition, the population spreading over 10 sites causes the incoherent component of purity to be significantly smaller than in the case of a TLS, leading to lower purity values under similar conditions.

With moderate site-bath coupling and at the higher temperature of Fig. 3c, the purity decreases monotonically and reaches a lower long-time value, which is only slightly larger than the minimum value for a 10-state system of 0.1.

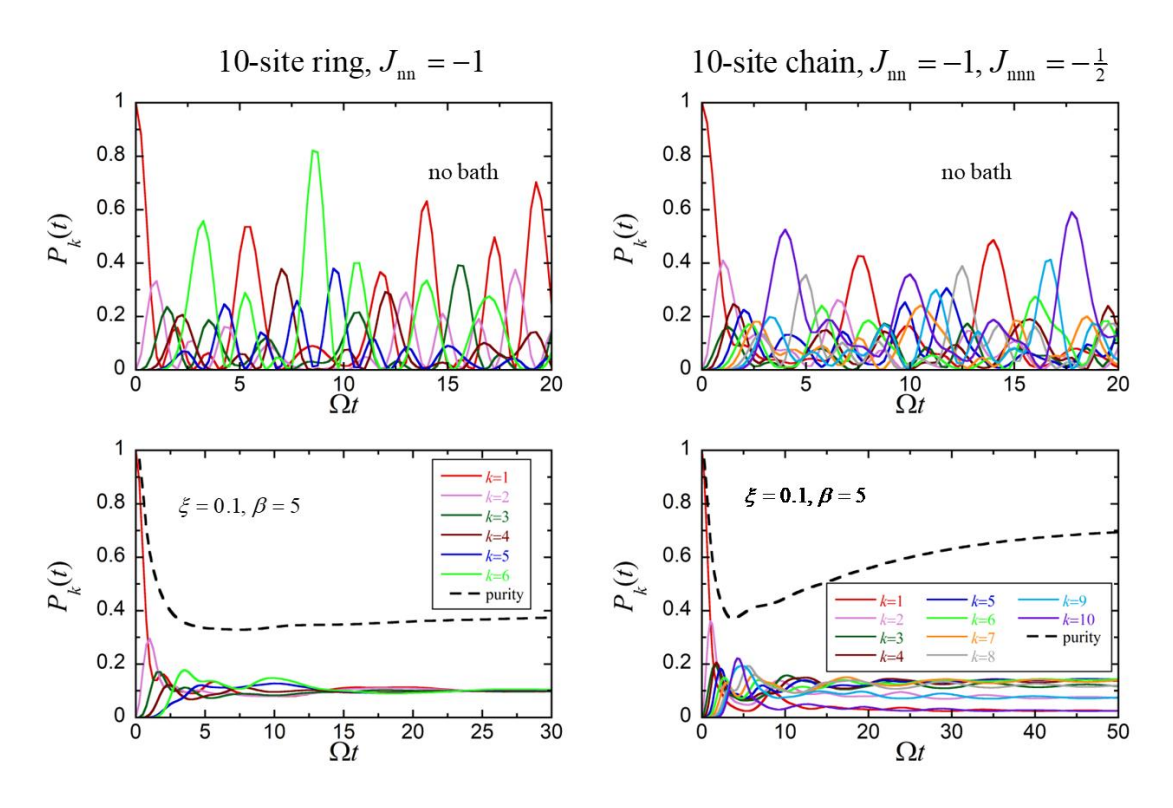


Fig. 7. Site populations as a function of time for a 10-site ring and a chain. The first site is populated initially. Left: ring with nearest-neighbor couplings of strength $J_{nn}=-1$. Right: chain with nearest-neighbor couplings of strength $J_{nn}=-1$ and next-nearest neighbor couplings $J_{nn}=-0.5$. Top: isolated system. Bottom: system coupled to a harmonic dissipative bath with $\xi=0.1$, $\beta=5$.

(ii) Effects of electronic structure and topology: Circular J aggregates and linear H aggregates

Next, we examine the manifestations of circular topology, which is found in light harvesting complexes, and different types of electronic couplings in the system Hamiltonian. Figure 7 shows the population dynamics for a 10-site circular J aggregate with nearest-neighbor couplings, as well as a linear aggregate with nearest- and next-nearest-neighbor couplings, with the parameters given earlier, for the isolated system and in the presence of weakly coupled baths at low temperature. The coherence maps are shown in Figures 8-10.

With circular (ring) boundary conditions, the coherence map has the topology of a torus. The topological effects are clearly identified in the coherence maps, as they give rise to symmetries in the directions of both diagonals passing from the initially populated site. This intrinsic symmetry is unaffected by dissipative interactions. Further, the ring topology creates two equivalent pathways, which interfere and lead to population accumulation diametrically opposite to the initially populated site. While damping effects of the bath reduce the buildup of population on that site, symmetry relations persist and give rise to intricate structures in Figures 8 and 9.

Figure 10 shows the coherence map for a 10-site J aggregate with weakly coupled, low-temperature baths with parameters similar to those of Fig. 5, but for a Hamiltonian that includes next-nearest-neighbor couplings. The introduction of additional couplings gives rise to new time scales in the population evolution, which are seen more clearly in Fig. 7. The most striking feature of the coherence map is the larger spread of nonzero elements in the direction perpendicular to the population line. This spread indicates stronger coherence compared to the case of only nearest-neighbor couplings. Not only are these coherence features robust, but they are amplified as time progresses and prevail at equilibrium. In fact, Fig. 10 shows that the band in the real part fills almost the entire RDM at equilibrium. The larger spread of coherences helps prevent purity loss in this case. Its minimum value is somewhat larger than the corresponding value in the absence of next-nearest-neighbor couplings with similar parameters (Fig. 3b), but its rebound is much more pronounced, exceeding 0.7 at long times.

Next, we explore the RDM evolution for a system Hamiltonian with positive site-to-site couplings. While not as common, such situations are encountered in certain aggregates and supramolecular structures. One of the most notable examples is the B850 ring of the LH2 complex, where the arrangement of the bacteriochlorophyll units leads to H-type nearest-neighbor coupling terms. Besides flipping the signs of the eigenstates, positive coupling values were recently found to give rise to intriguing dynamical effects in excitonic Hamiltonians with a dendrimer topology, which were attributed to electronic frustration. Here we examine the time evolution of coherence maps for a 10-site chain weakly coupled to a low-temperature bath with parameters to those in Fig. 5, but with $J_{\rm nn}=+1$. In this frustration-free system, the population evolution is very similar to that shown in the middle panel of Fig. 4.

The coherence map for the same parameters is shown in Figure 11. While the magnitude and spread of real and imaginary parts are very similar to those shown in Fig. 5, both real and imaginary parts now exhibit frequent sign changes, and the equilibrium RDM is characterized by bands of alternating signs, which reflect the structure of the ground state.

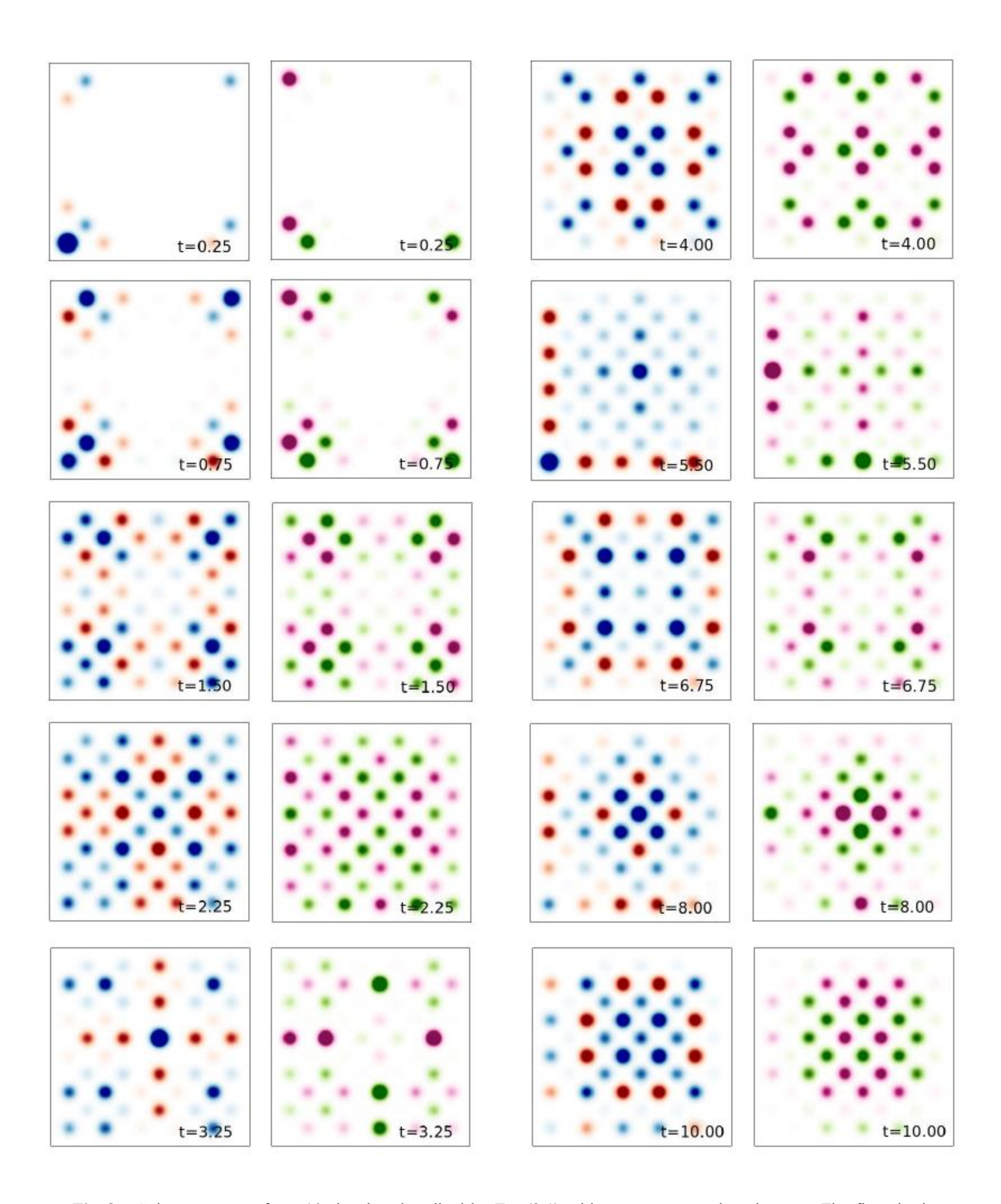


Fig. 8. Coherence maps for a 10-site ring described by Eq. (3.1) with $J_{\rm nn}=-1$ at various instants. The first site is initially populated. Blue and red colors correspond to positive and negative areas of the real part of the RDM, while magenta and green correspond to positive and negative areas of the imaginary part of the RDM.

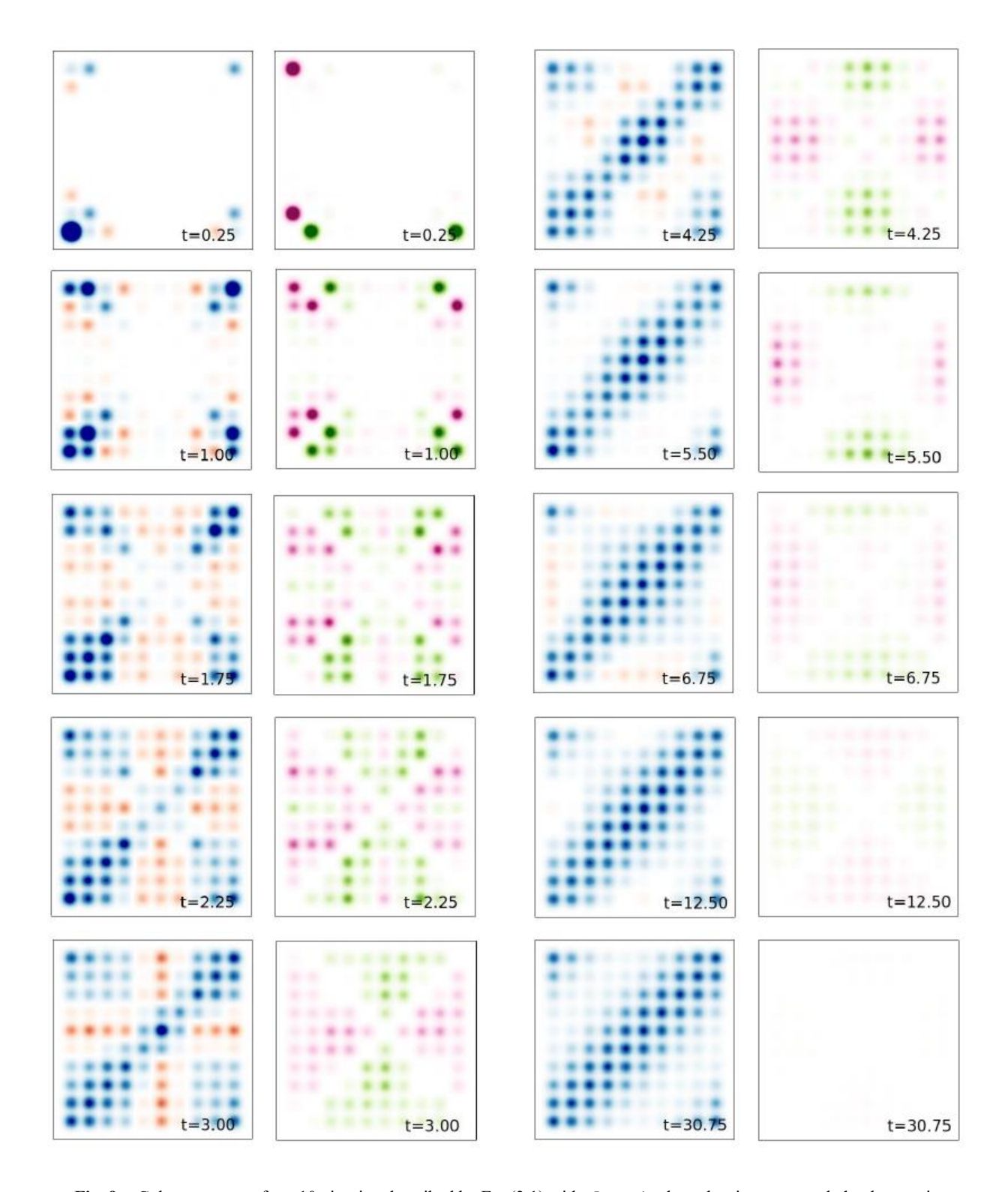


Fig. 9. Coherence maps for a 10-site ring described by Eq. (3.1) with $J_{\rm nn}=-1$ where the sites are coupled to harmonic baths with $\xi=0.1$ at an inverse temperature $\beta=5$, at various instants. The first site is initially populated. Blue and red colors correspond to positive and negative areas of the real part of the RDM, while magenta and green correspond to positive and negative areas of the imaginary part of the RDM.

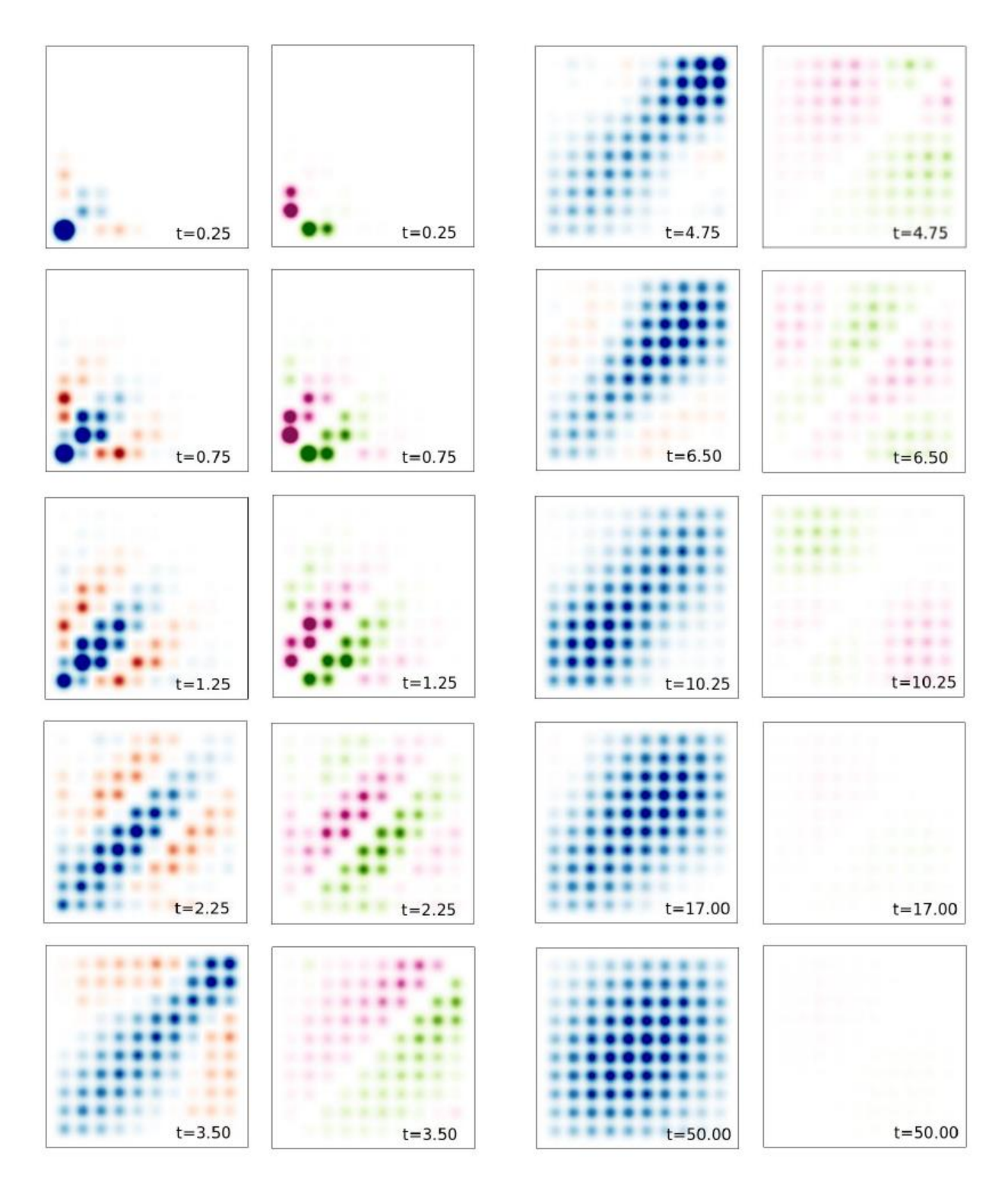


Fig. 10. Coherence maps for a 10-site chain described by Eq. (3.1) with $J_{nn}=-1$ and $J_{nnn}=-0.5$ where the sites are coupled to harmonic baths with $\xi=0.1$ at an inverse temperature $\beta=5$, at various instants. The first site is initially populated. Blue and red colors correspond to positive and negative areas of the real part of the RDM, while magenta and green correspond to positive and negative areas of the imaginary part of the RDM.

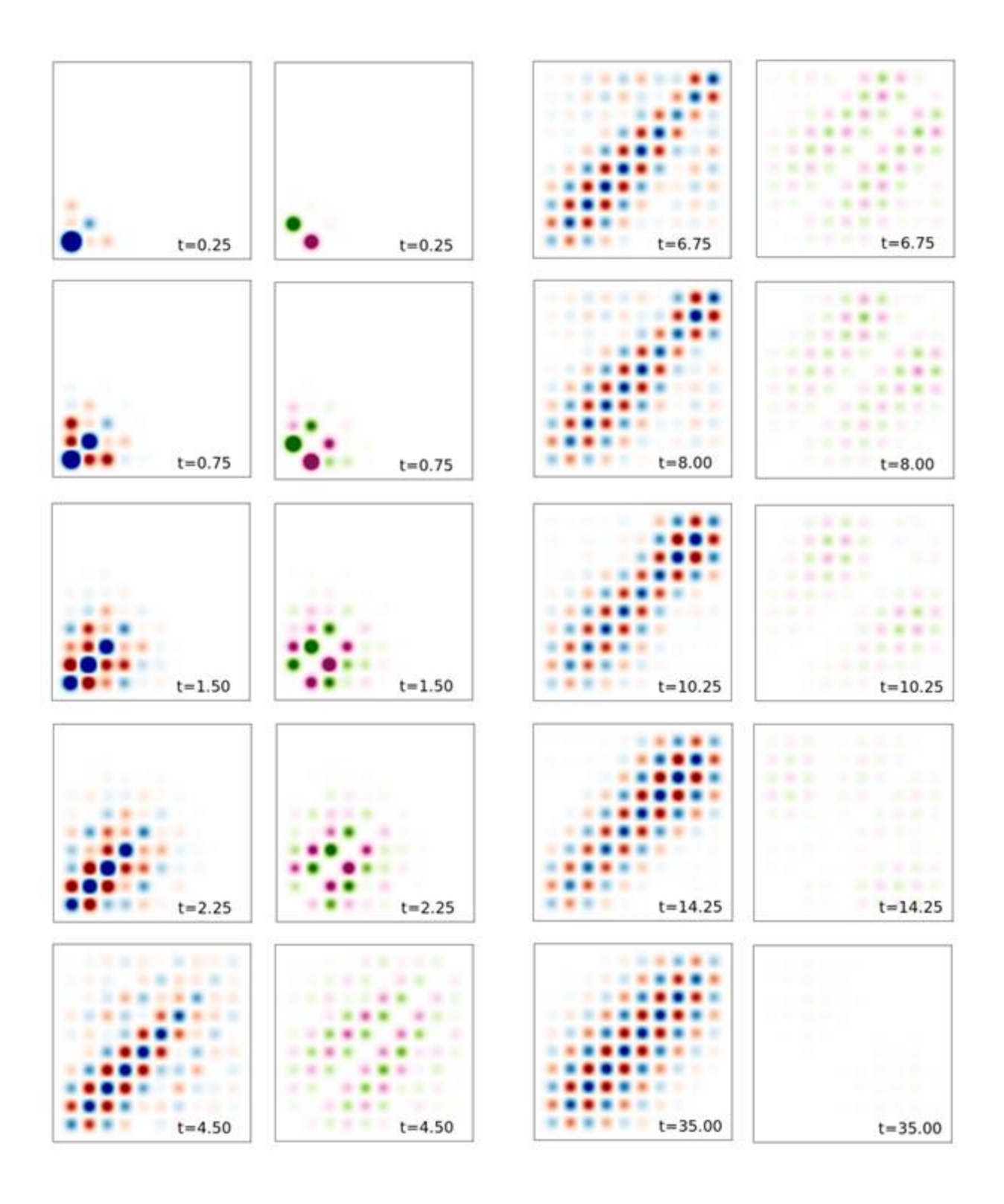


Fig. 11. Coherence maps for a 10-site chain described by Eq. (3.1) with $J_{nn} = +1$ where the sites are coupled to harmonic baths with $\xi = 0.1$ at an inverse temperature $\beta = 5$, at various instants. The first site is initially populated. Blue and red colors correspond to positive and negative areas of the real part of the RDM, while magenta and green correspond to positive and negative areas of the imaginary part of the RDM.

(iii) Eigenstate initial condition

Last, we explore the coherence map obtained with an initial RDM that corresponds to an excited eigenstate of the system Hamiltonian. In this case there is no evolution in the absence of system-bath coupling. Figures 12 and 13 show the time evolution of the site populations and the coherence map for a 10-site linear aggregate with $J_{\rm nn}=-1$, whose sites are weakly coupled to low-temperature baths, with the initial excitation on the highest eigenstate of the system Hamiltonian. The long-time values of the site populations reflect the participation of the various sites in the eigenstates, primarily the ground state at this low temperature. The edge states are seen to have lower population values at equilibrium than interior sites.

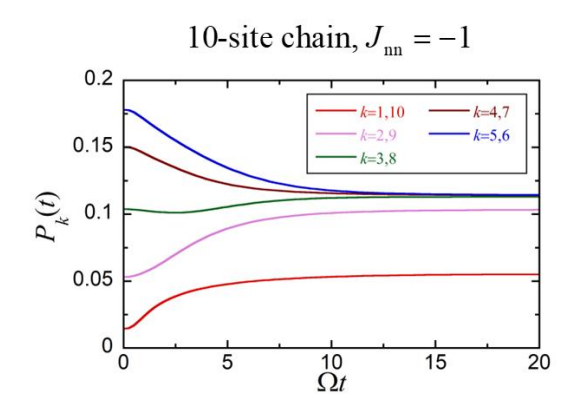


Fig. 12. Site populations as a function of time in a 10-site chains with nearest-neighbor couplings of strength $J_{\rm nn}=-1$, where the sites are coupled to harmonic dissipative baths with $\xi=0.1$, $\beta=5$.

The eigenstate initial condition leads to a coherence map which is initially spread over all sites, and the alternating signs of this high-energy eigenstate are reflected in the coherence map. Because the time evolution is much slower compared to that with a site-localized initial condition, the imaginary components of the coherences have considerably smaller values compared to those in the similar system shown in Fig. 5. The symmetric nature of the eigenstate introduces a second symmetry line perpendicular to the principal diagonal.

During the very early stage of the evolution, the real part of the RDM localizes primarily about the population line. Imaginary components appear mostly along the lines parallel to the main diagonal as well. As time progresses, the RDM is seen to spread again, filling lines parallel to the principal diagonal, both in the real and imaginary components. As the dynamics begins to approach equilibrium the real-valued band continues to broaden while the imaginary elements fade to zero. Eventually, the coherence map becomes identical to that obtained with a site initial condition (Fig. 5).

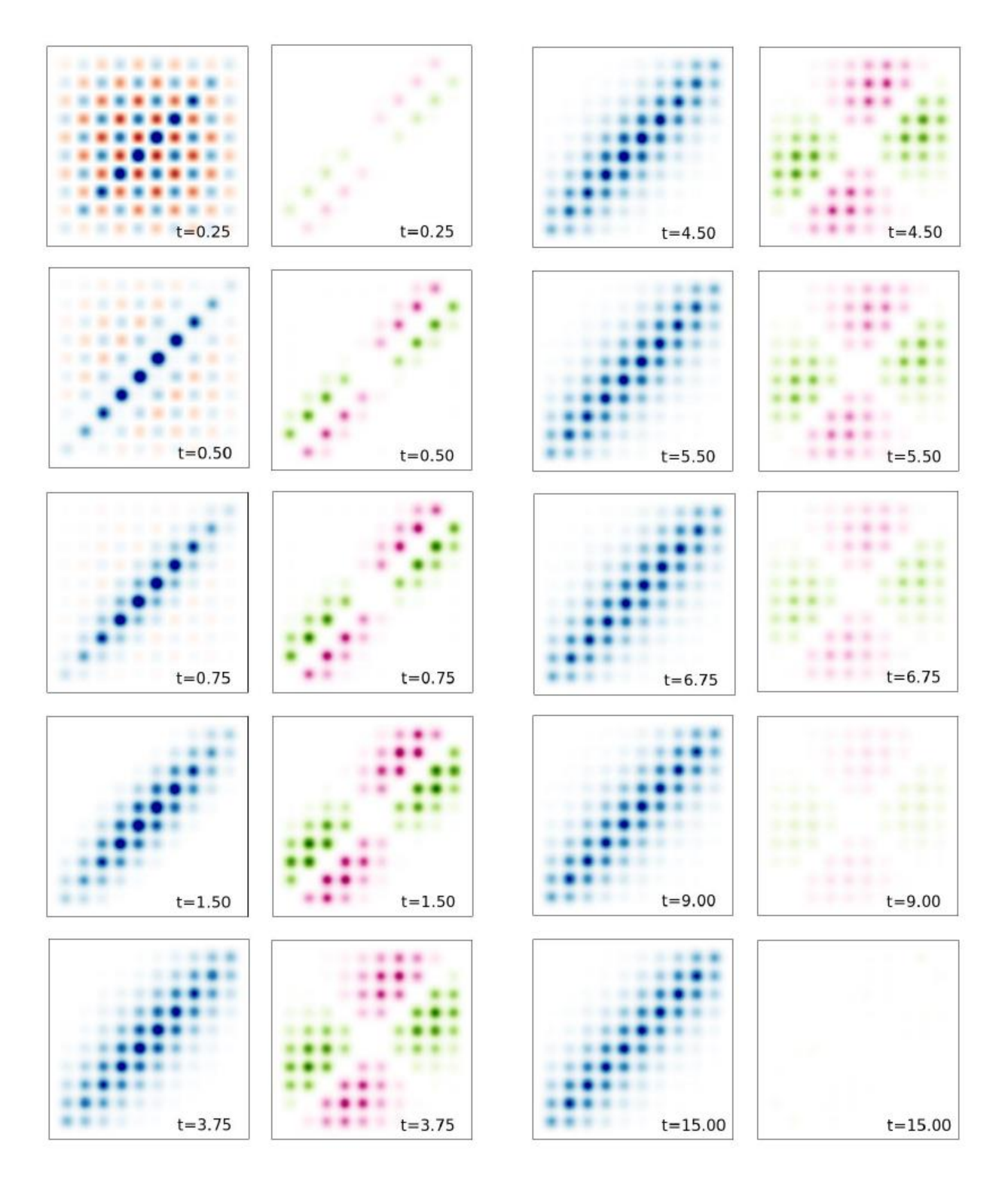


Fig. 13. Coherence maps for a 10-site chain described by Eq. (3.1) with $J_{nn} = -1$ where the sites are coupled to harmonic baths with $\xi = 0.1$ at an inverse temperature $\beta = 5$, at various instants. The highest energy eigenstate of the system Hamiltonian is initially excited. Blue and red colors correspond to positive and negative areas of the real part of the RDM, while magenta and green correspond to positive and negative areas of the imaginary part of the RDM. In this figure the imaginary component was very small, so it is shown multiplied by 10 for clarity.

4. Concluding Remarks

The time evolution of the entire RDM, captured most transparently and effectively through coherence maps, encodes rich information related to the dynamics of a system and the state of equilibrium. The coherence map of isolated systems is highly structured and reflects the topological features and symmetry properties of the system's Hamiltonian. In the case of a pure state, coherences convey the site amplitudes of quantum state superpositions, and all rows and columns of the RDM contain the same information. Thermal effects and dissipative interactions mix quantum superpositions, destroying unitary, decreasing purity and washing out coherences.

The imaginary components of the coherences determine the instantaneous rates of population change. Such terms emerge in the very early steps of the dynamics and grow to significant values if the populations oscillate rapidly, eventually decaying to zero as the system reaches the real-valued Boltzmann distribution. The real components of the RDM display intricate patterns at short times, followed by a gradual localization along the principal diagonal. Fluctuations in both directions (along and perpendicular to the population line) are observed as the system approaches equilibrium. The real-valued RDM eventually forms a band whose width is governed by the interplay among dissipation strength, thermal fluctuations and site-to-site coupling terms.

Besides discussing the various relationships and characteristics of RDM elements, we have presented snapshots of coherence maps for 10-state tight binding systems with the topology of chains and rings, with nearest-neighbor and with additional next-nearest-neighbor couplings, for negative and positive coupling values, with site-localized and eigenstate initial conditions, in isolation or in contact with harmonic baths of weak and moderate dissipation strength as well as at low and intermediate temperatures, using parameters characteristic of Frenkel exciton-type molecular aggregates. Because "a picture is worth a thousand words", the visual examination of these image collections for several representative models conveys these relations effectively and clearly, offering valuable insights for understanding the dynamics of complex multistate systems.

Acknowledgments

This material is based upon work supported by the National Science Foundation under Award CHE-1955302.

References

- 1. Jonas, D. M., Two-dimensional femtosecond spectroscopy. *Annu. Rev. Phys. Chem.* **2003**, *54*, 425-463.
- 2. Brixner, T.; T., M.; Stiopkin, I. V.; Fleming, G. R., Phase-stabilized two-dimensional electronic spectroscopy *J. Chem. Phys.* **2004**, *121*, 4221.
- 3. Dean, J. C.; Scholes, G. D., Coherence Spectroscopy in the Condensed Phase: Insights into Molecular Structure, Environment, and Interactions. *Accounts of Chemical Research* **2017**, *50* (11), 2746-2755.
- 4. Jonas, D. M., Vibrational and Nonadiabatic Coherence in 2D Electronic Spectroscopy, the Jahn–Teller Effect, and Energy Transfer. *Annual Review of Physical Chemistry* **2018**, *69* (1), 327-352.
- 5. Olivera, T. A. A.; Lewis, N. H. C.; Fleming, G. R., Correlating the motion of electrons and nuclei with two-dimensional electronic–vibrational spectroscopy *Proc. Nat. Acad Sci. USA* **2014**, *111*, 10061-10066.
- 6. Mukamel, S., *Principles of nonlinear optical spectroscopy*. Oxford University Press: New York, 1995.
- 7. Cina, J. A., *Getting Started on Time-Resolved Molecular Spectroscopy*. Oxford University Press: Oxford, 2022.
- 8. Blum, K., *Density matrix theory and applications*. Plenum: New York.
- 9. Schatz, G. C.; Ratner, M. A., *Quantum mechanics in chemistry*. Prentice Hall: Englewood Cliffs, New Jersey, 1993.
- 10. Gordon, R. G., Correlation functions for molecular motion. *Advances in Magnetic and Optical Resonance* **1968**, *3*, 1-42.
- 11. Onsager, L., Reciprocal Relation in Irreversible Processes II. *Phys. Rev.* **1931,** *38*, 2265-2279.
- 12. Chandler, D., *Introduction to Modern Statistical Mechanics*. Oxford University Press: New York, 1987.
- 13. Kubo, R.; Toda, M.; Hashitsume, N., *Statistical Physics*. 2nd ed.; Springer-Verlag: Heidelberg, 1991; Vol. 2.
- 14. Yamamoto, T., Quantum Statistical Mechanical Theory of the Rate of Exchange Chemical Reactions in the Gas Phase. *J. Chem. Phys.* **1960**, *33*, 281-289.
- 15. Redfield, A. G., On the theory of relaxation processes. *IBM Journal of Research and Development* **1957**, *I*, 19-31.
- 16. Feynman, R. P., Space-time approach to non-relativistic quantum mechanics. *Rev. Mod. Phys.* **1948,** *20*, 367-387.
- 17. Feynman, R. P.; Hibbs, A. R., *Quantum Mechanics and Path Integrals*. McGraw-Hill: New York, 1965.
- 18. Dani, R.; Makri, N., Quantum State-to-State Rates for Multistate Processes from Coherences. *The Journal of Physical Chemistry Letters* **2022**, *13* (34), 8141-8149.
- 19. von Neumann, J., *Mathematical foundations of quantum mechanics*. Princeton University Press: 1955.
- 20. Chatterjee, S.; Makri, N., Density matrix and purity evolution in dissipative two-level systems: I. Theory and path integral results for tunneling dynamics. *Phys. Chem. Chem. Phys.* **2021**, *23*, 5113-5124.
- 21. Chatterjee, S.; Makri, N., Recovery of purity in dissipative tunneling dynamics. *J. Phys. Chem. Lett.* **2020,** *11*, 8592-8596.
- 22. Chatterjee, S.; Makri, N., Density matrix and purity evolution in dissipative two-level systems: II. Relaxation dynamics. *Phys. Chem. Chem. Phys.* **2021**, (23), 5125-5133
- 23. Frenkel, J., On the transformation of light into heat in solids. *Phys. Rev.* **1931,** *37*, 17.
- 24. May, V.; Kuhn, O., Theory of charge and energy transfer in molecular systems. Wiley: 1999.
- 25. Hestand, N. J.; Spano, F. C., Expanded Theory of H- and J-Molecular Aggregates: The Effects of Vibronic Coupling and Intermolecular Charge Transfer. *Chemical Reviews* **2018**, *118* (15), 7069-7163.

- 26. Nalbach, P.; Eckel, J.; Thorwart, M., Quantum coherent biomolecular energy transfer with spatially correlated fluctuations. *New Journal of Physics* **2010**, *12*, 065043.
- 27. Kundu, S.; Makri, N., Intramolecular vibrations in excitation energy transfer: Insights from real-time path integral calculations. *Annual Review of Physical Chemistry* **2022**, *73* (1), 349-375.
- 28. Caldeira, A. O.; Leggett, A. J., Path integral approach to quantum Brownian motion. *Physica A* **1983,** *121*, 587-616.
- 29. Leggett, A. J.; Chakravarty, S.; Dorsey, A. T.; Fisher, M. P. A.; Garg, A.; Zwerger, M., Dynamics of the dissipative two-state system. *Rev. Mod. Phys.* **1987**, *59*, 1-85.
- 30. Tretiak, S.; Middleton, C.; Chernyak, V.; Mukamel, S., Exciton Hamiltonian for the bacteriochlorophyll system in the LH2 antenna complex of purple bacteria. *J. Phys. Chem. B* **2000,** *104*, 4519-4528.
- 31. Ambrosek, D.; Köhn, A.; Schulze, J.; Kühn, O., Quantum Chemical Parametrization and Spectroscopic Characterization of the Frenkel Exciton Hamiltonian for a J-Aggregate Forming Perylene Bisimide Dye. *The Journal of Physical Chemistry A* **2012**, *116* (46), 11451-11458.
- 32. Li, X.-Q.; Zhang, X.; Ghosh, S.; Würthner, F., Highly Fluorescent Lyotropic Mesophases and Organogels Based on J-Aggregates of Core-Twisted Perylene Bisimide Dyes. *Chemistry A European Journal* **2008**, *14* (27), 8074-8078.
- 33. Makri, N., Small matrix disentanglement of the path integral: overcoming the exponential tensor scaling with memory length. *J. Chem. Phys.* **2020**, *152*, 041104.
- 34. Makri, N., Small matrix path integral for system-bath dynamics. *Journal of Chemical Theory and Computation* **2020**, *16*, 4038–4049.
- 35. Makri, N., Small matrix path integral with extended memory. *J. Chem. Theory and Comput.* **2021**, *17*, 1-6.
- 36. Makri, N., Improved Feynman propagators on a grid and non-adiabatic corrections within the path integral framework. *Chem. Phys. Lett.* **1992**, *193*, 435-444.
- 37. Makri, N.; Makarov, D. E., Tensor multiplication for iterative quantum time evolution of reduced density matrices. I. Theory. *J. Chem. Phys.* **1995**, *102*, 4600-4610.
- 38. Makri, N.; Makarov, D. E., Tensor multiplication for iterative quantum time evolution of reduced density matrices. II. Numerical methodology. *J. Chem. Phys.* **1995**, *102*, 4611-4618.
- 39. Makri, N., Numerical path integral techniques for long-time quantum dynamics of dissipative systems. *J. Math. Phys.* **1995,** *36*, 2430-2456.
- 40. Feynman, R. P.; Vernon, F. L., The theory of a general quantum system interacting with a linear dissipative system. *Ann. Phys.* **1963**, *24*, 118-173.
- 41. Dani, R.; Makri, N., Excitation Energy Transfer in Bias-Free Dendrimers: Eigenstate Structure, Thermodynamics, and Quantum Evolution. *The Journal of Physical Chemistry C* **2022**, *126* (25), 10309-10319.